

# Mapping Comfort with the SMART (Spherical Motion Average Radiant Temperature) Sensor

Eric Teitelbaum<sup>1</sup>, Hongshan Guo<sup>2</sup>, Jake Read<sup>3</sup>, Forrest Meggers<sup>2,4</sup>

<sup>1</sup>Princeton University, Civil and Environmental Engineering, Princeton, NJ, USA

<sup>2</sup>Princeton University, School of Architecture, Princeton, NJ, USA

<sup>3</sup>University of Waterloo, Waterloo Architecture, Cambridge, ON, CAN

<sup>4</sup>Princeton University, Andlinger Center for Energy and the Environment, Princeton, NJ, CAN

## Abstract

The understanding of thermal comfort has improved significantly since the introduction of the Fanger comfort model (1970), yet Predicted Mean Vote (PMV) and its adapted versions still are the predominantly used forms (Rupp et al., 2015). Out of the six variables contributing to the PMV values and occupant thermal comfort, Mean Radiant Temperature (MRT) and radiant exchanges account for up to half of an occupant's net heat loss. To better model the relationship between the human body and the radiant temperatures, a device to measure the MRT throughout an occupied space is required. This is a currently relevant piece of equipment as the number of radiant heating and cooling systems is increasing not only in the United States, but all around the world (Lin et al., 2016). We present the development and implementation of the SMART (Spherical Motion Average Radiant Temperature) Sensor as a means to improve available data and representation of comfort in building spaces.

## Introduction

Mean radiant temperature is one of the most important metrics related to thermal conditions, and is defined as the uniform temperature of a hypothetical spherical surface surrounding the subject (emissivity  $\epsilon=1$ ) that would result in the same net radiation energy exchange with the subject as with the actual radiative environment surrounding the occupant. The determination of the actual mean radiant temperature, however, remains a major challenge, and when surface temperature information is not known standard practice has the MRT set to the air temperature. Globe thermometers, such as black globe thermometers, are usually considered accurate with the air velocity under  $0.1 \text{ m/s}$ , as higher airflow around the black globe thermometer leads to convective heat loss or gain to the globe, thus resulting in disturbances in estimating the globe temperature. For perspective, a  $0.1 \text{ m/s}$  error in velocity measurement with a  $15\text{cm}$  globe at a  $5^\circ\text{C}$  difference between air and globe can result in a  $1.6^\circ\text{C}$  error in the calculated mean radiant temperature. There are empirical relationships to correct for convective losses with a

known air velocity, however these relationships are often subject to high temporal lags. The actual measurement becomes more problematic in outdoor conditions as wind is unpredictable and variable. Lidwell and Wyon (1968) as well as McIntyre (1976) have reported cases where the black globe thermometer can also be shaded with either a polyethylene shield, or multiple unheated spheres with equal emissivities to determine the MRT. To understand the radiative flux between different surfaces, radiometers were also used to measure the radiation for thermal comfort assessment. Berglund (1977) categorized all radiation measurements into radiometers, dividing them into two classes, active and passive: active in the sense that they supply or remove energy from the sensor. The globe thermometer developed by Vernon (Bedford, T and Warner, C G, 2009) can therefore be categorized as the first and simplest passive radiometer.

Active radiometers, on the other hand, include powered components that keep the sensor at the ambient and air temperature. Radiometers heated to above the ambient temperature can be found in examples such as the Panradiometer developed by Richards, Stoll and Hardy (1951) to measure the mean long wave radiation temperature and solar or high temperature radiation intensity and has the benefit of independence from air velocity by using three globes of same geometry but different absorptive types and emissivities. Sutton and McNall (Koch, 1961) improved the Panradiometer in terms of accuracy and sensitivity to drafts and downsized to two spheres instead of three. Gagge et al. (1967) developed the R-Meter, measuring the operative temperature (Halawa, Edward et al., 2014), which is defined as the temperature of an imaginary enclosure which exchanges the same total dry heat by radiation and convection as the actual environment with a operational temperature. Aagard designed a globe to measure the MRT of the cold night sky, where the radiant temperature is always colder than the air temperature, and was measurable with black globe made from single layer of No. 36 enameled Constantan wire (Aagard, 1958). A directional radiometer was proposed by Korsgaard that is analogous to mean radiant temperature, but with a sensitive net radiometer, it is possible

to obtain mean radiant temperature (Korsgaard, V, 1949).

Similarly, Hager (1963) developed an Absolute Differential Radiometer that can be used without calibration. Berglund concluded that what an engineer would need is a fast-acting, rugged, reasonably priced MRT indicator for field survey work. More modern approaches have used advanced linear regression models (Spagnolo and De Dear, 2003) and three-axis short- and long-wave radiometers (Thorsson et al., 2007) to measure MRT in outdoor environments without needing to correct for wind, however these are values for only a single location in space where the sensor is placed.

To continue this work among radiant sensing technologies, our group has developed the SMART (Spherical Motion Average Radiant Temperature) sensor which takes the radiant measurement together with the space geometry, producing a spatially unique calculation of mean radiant temperature. As the readings are only of the surface temperature, it is insensitive to convective losses and allows quick diagnosis of surrounding surfaces' radiant heat exchange with the occupants. Distance measurements allow the MRT to be calculated at any point within the space, rather than only at the location of the sensor.

## Methods

The general principle behind the sensor's operation is to scan a space with both a rangefinder and a temperature sensor to map each surface temperature, subdivided by the field of view (FOV) of the temperature sensor to minimize overlap in the datapoints. (Eventually, statistical analyses could help explore oversampling to get a more precise dataset.) Doing so allows spatial information to be recorded with the temperature information overlaid, allowing the MRT to be calculated exactly at the location of the measurement, as provided by a black globe thermometer at air velocities less than  $0.1m/s$ , but more importantly the MRT can also be measured at any point without occlusion in the room. The sensor does this from its geometry measurements combined with a novel set of post processing algorithms that will be fully described in this section.

### Surface Temperature Data Collection

The sensor consists of a Melexis 5° field of view non-contacting infrared temperature sensor and a Lidar-Lite rangefinder module, which are both always oriented along the same vector. Additionally there are two servos that swing both sensors through space, with one servo rotating the sensor platform along the central rotational axis,  $\theta$ , from 0 to  $180^\circ$ , and the other servo moving just the rangefinder and temperature sensor elements along the angle of inclination,  $\phi$ , from 0 to  $360^\circ$ . Figure 1 shows a photo of the completed sensor prototype. The binocular device is the LidarLite module, and the smaller sensor is the

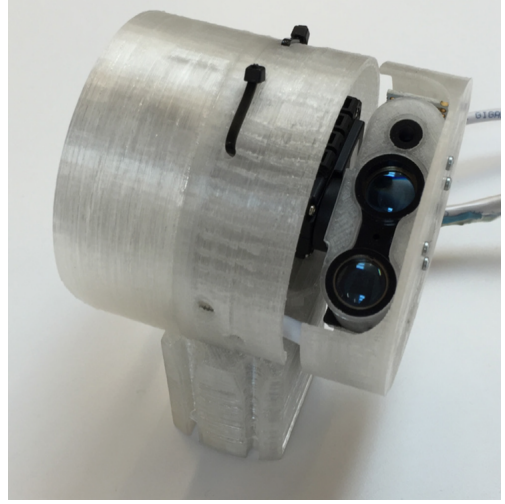


*Figure 1: A photograph of the completed sensor. The binocular type sensor is the LidarLite rangefinder module and the smaller circle is the Melexis 5° FOV non-contacting surface temperature sensor.*

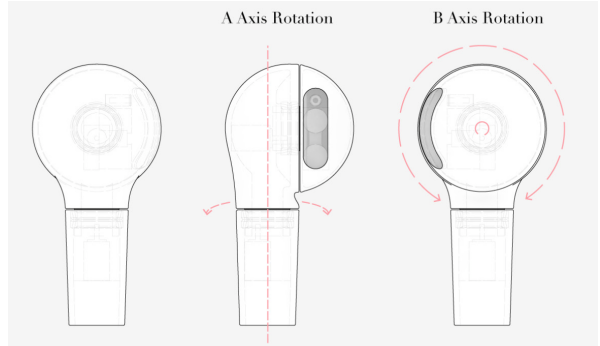


*Figure 2: A diagram of the completed sensor showing the two axes of rotation.*

### Melexis 5° field of view temperature sensor.

The first rotational servo which rotates the A axis pictured in figure 2 rotates the entire sensor body by the FOV,  $\delta$  of the temperature sensor, and then the second servo moves the rangefinder and temperature sensor elements in increments of  $\delta$  in the B axis. The sensor's motion in degrees,  $\phi_{motion}$ , between readings is calculated based on the current value of the rotational servo and  $\delta$  given in equation 1. With this calculation, the number of points is reduced compared to an algorithm that captures data for a fixed value of  $\phi$ .

$$\phi_{motion} = 360 \left( \frac{\tan(\frac{\delta}{2})}{\pi \cos \theta} \right) \quad (1)$$

Once axis B has moved from 0 to  $360^\circ$ , axis A again rotates by  $\theta = \delta$ . Now axis B rotates  $\phi$  from  $360$  to  $0^\circ$  recording points. A full reading is completed when axis A has traversed  $\theta = 180^\circ$ . Such motion obtains a geodesic distribution of points. Unfortunately, the geodesic distribution must be sacrificed if the point

Table 1: Structure of the data recorded by the sensor.

	$\theta_i$	$\theta_{i+1}$	$\theta_m$
$\phi_j$	$(r_{i,j}, T_{i,j})$	$(r_{i+1,j}, T_{i+1,j})$	$(r_{m,j}, T_{m,j})$
$\phi_{j+1}$	$(r_{i,j+1}, T_{i,j+1})$	...	...
$\phi_n$	$(r_{i,n}, T_{i,n})$	...	$(r_{m,n}, T_{m,n})$

cloud is required to fit in a rectangular matrix, a condition for triangulation in later steps. A rectangular matrix is defined by fixed angular motion of the servos, creating overlapping datapoints especially at the top and bottom of the imaginary sphere of datapoints. These need to be weighted using a weighting factor  $\mu$  provided in equation 2. The rectangular matrix was used for all datasets reported in this paper.

$$\mu = \frac{1}{2} \cos(\phi) - \cos(\phi + \delta) \quad (2)$$

Each sensor measurement records the angular position of each servo,  $\theta$  and  $\phi$ , as well as the range,  $r$ , and temperature,  $T$ . The data matrix is shown in table 1.

Without any processing, this dataset is sufficient to take this sphere of data points and plot it in 2D. Temperatures at the top and bottom are exaggerated, just like when the spherical surface of the planet is mapped on a rectangular chart, but features are recognizable nonetheless. This flattened 2D image and accompanying dataset can immediately be used to calculate the MRT at the location from the sensor, and to plot the influences of MRT in specified directions around a space to find disturbances from particular surfaces.

### Geometric Parameterization

From the completed data matrix shown in table 1, the 2D temperature information can be used to reconstruct a 3D point cloud of the room when coupled with the Lidar distance information. Since each servo angle and temperature measurement also have an accompanying distance measurement, the 3D point cloud of the surfaces in the room is achieved by plotting each spherical coordinate of the form  $(\theta, \phi, r)$  to  $(x, y, z)$  Cartesian coordinates and then plotted on a 3D set of axes. Additionally, the color of each point is picked to correspond to the temperature reading associated at each point, a 4th dimension. In this way, a 3D thermal map of the surfaces of the room is generated with the data taken from the SMART Sensor.

To fully parametrize the geometry based on point cloud data, the point cloud must be enclosed into a volume with each 2x2 matrix cell being diagonalized from  $i, j$  to  $i + 1, j + 1$ , forming 2D triangles defined by the points  $(\theta_{i,j}, \phi_{i,j}, r_{i,j}), (\theta_{i,j+1}, \phi_{i,j+1}, r_{i,j+1}), (\theta_{i+1,j+1}, \phi_{i+1,j+1}, r_{i+1,j+1})$  for the lower triangle, and  $(\theta_{i,j}, \phi_{i,j}, r_{i,j}), (\theta_{i+1,j}, \phi_{i+1,j}, r_{i+1,j}),$

$(\theta_{i+1,j+1}, \phi_{i+1,j+1}, r_{i+1,j+1})$  for the upper triangle. The vertices of each triangle has an associated temperature measurement.

### Spatially-resolved MRT Calculation

Once the triangulation is performed, surfaces have now been established that represent unique fields of view for an occupant positioned in different locations within the room. The field of view changes when an occupant moves, based on an occupant's proximity to a surface. Knowing the geometry of the space allows precise calculation of the view factor. The view factor for each subdivided surface element is important since physically, the MRT a hypothetical uniform environment, one that is different depending on occupant location. Specifically, the solid angle subtended by each surface triangle must be calculated for each position in the room as part of determining the MRT over the entire space in the room. Figure 3 is a diagram of how the solid angle subtended by fixed points A, B, and C changes at different points,  $O_1$ ,  $O_2$ , and  $O_3$ . For a single point, say  $O_1$ , the 2D angles  $\theta_{AO_1B}$ ,  $\theta_{BO_1C}$ , and  $\theta_{AO_1C}$  are required. Matlab® has two built-in functions, atan2 and norm, that calculate the angle between any two 3D vectors  $\vec{O_1A}$  and  $\vec{O_1B}$  from the Euclidian norm of a vector. Equation 3 shows the relationship used to calculate each angle.

$$\theta = \text{atan2}(\text{norm}(\vec{a} \times \vec{b}), \vec{a} \cdot \vec{b}) \quad (3)$$

Using the known coordinates of A, B, and C vertices, vectors from point  $O_1$  are calculated through each of these points and plugged into equation 3. This returns values for  $\theta_{AO_1B}$ ,  $\theta_{BO_1C}$ , and  $\theta_{AO_1C}$ . L'Huilier's theorem is invoked to calculate the solid angle subtended by the triangle using these three angles. First,  $\theta_s$  is calculated as shown in equation 4.

$$\theta_s = \frac{\theta_{AO_1B} + \theta_{BO_1C} + \theta_{AO_1C}}{2} \quad (4)$$

Next, the solid angle,  $\Omega$ , is calculated using equation

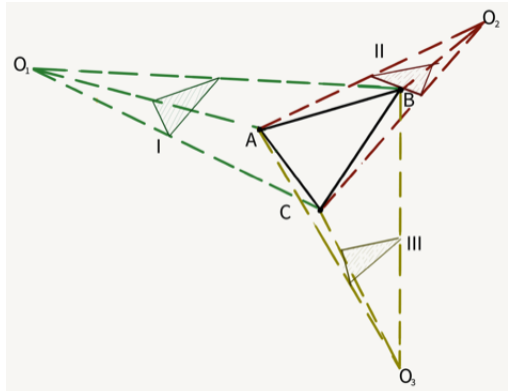


Figure 3: A diagram of the change in solid angle subtended by fixed points A, B, and C at different points,  $O_1$ ,  $O_2$ , and  $O_3$ .

5.

$$\Omega = 4 \tan^{-1} \left[ \left( \tan \left( \frac{\theta_S}{2} \right) \times \tan \left( \frac{\theta_S - \theta_{AO_1B}}{2} \right) \times \tan \left( \frac{\theta_S - \theta_{BO_1C}}{2} \right) \times \tan \left( \frac{\theta_S - \theta_{AO_1C}}{2} \right) \right)^{\frac{1}{2}} \right] \quad (5)$$

To calculate the average temperature within each triangle, the temperature reading at each corner is averaged and then multiplied by 1/6 to avoid double counting points in connected triangles.

Through this process one may take a point cloud, triangulate the cloud to produce a volume, and the solid angle by any triangle for any point in the room can now be calculated. This allows the MRT to be known at any point in the space from one reading. To produce plots of this result, the room is broken down into an  $xy$  grid of arbitrary granularity, and at each  $xy$  location the MRT is computed for a fixed  $z$  height. This creates slices of the MRT profile at fixed heights, varying throughout the  $xy$  coordinate space. Therefore the end result of the methodology is to create a MRT profile throughout the space defined in the room at any point and at any height. Through this approach, we present our results for calculating the mean radiant temperature at each point in a room from a single sensor reading.

## Results

### Surface Temperature Scanning

The simplest type of representation generated from the data created by the SMART sensor is a 2D graphic without range information, shown in figure 4. In this figure, the  $x$  and  $y$  axes correspond to the rotation of each servo in degrees. The gradient plot is therefore the measured temperature at each servo location, and the top line graph is the average of each column, which is again averaged to obtain a MRT at the sensor location of 24.2 °C. The color of each point corresponds to a temperature measurement assigned by the color bar. Hues towards the blue end of the spectrum are colder points, and temperatures get warmer as a point's color approaches dark red. The same color range is used for all sensor outputs in this paper.

### Geometric Parameterization

Once distance information is added, simple point clouds can be plotted, shown in figures 5 and 9. Here, the spherical coordinates  $(\theta, \phi, r)$  are transformed to Cartesian coordinates,  $(x, y, z)$ , and plotted. The distance reading is reporting the closest object in the sensor's 2° field of view. The next step is to triangulate the point cloud to begin determining the MRT at each location within the room. The triangulation is shown in figure 6. Figures 4, 5, and 6 are all of the

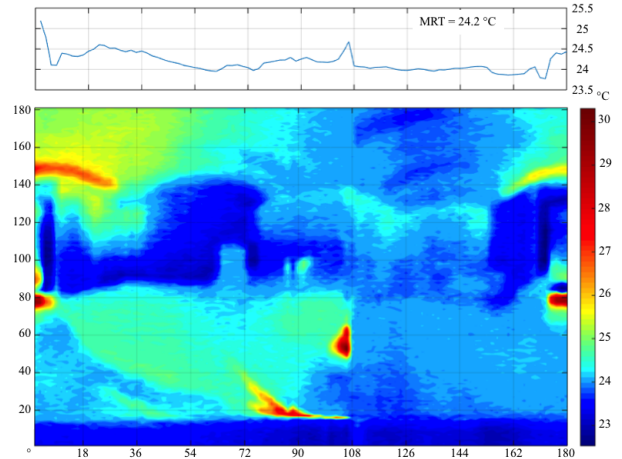


Figure 4: A 2D scan performed by the SMART sensor, without distance information. The lower gradient contour shows temperature information given by color at each servo angle. The top graph is a weighted average of each column, which is then averaged to obtain the MRT at the sensor location.

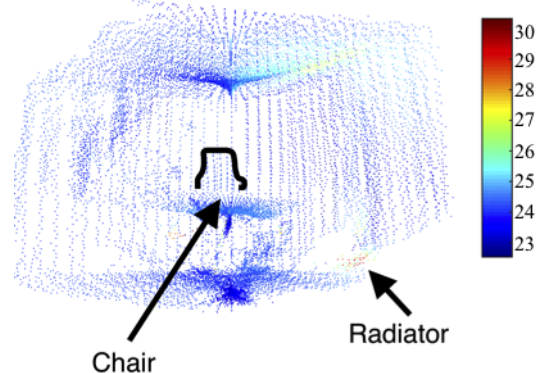


Figure 5: A 3D point cloud generated by the SMART sensor with features identified.

same space. Common features such as a prominent cold window and radiator underneath can be identified in each.

In figure 6, the  $x, y$ , and  $z$  axes units' are cm, and are defined with the sensor as the origin. The sensor was 1 m off the ground, and relatively equidistant from each wall.

### Spatially-resolved MRT Contours

Next, using the procedure outlined with equations 3-5, the MRT was calculated on a 20x20  $x, y$  grid within the room at 1m and 2m heights. The result was plotted in figure 7. This data is interpreted as the perceived MRT at each  $x, y$  position in the room at a fixed height of either 1 or 2 meters. Or put another way, the hypothetical uniform MRT environment as a function of position. These values come from the triangulation and view factor calculation algorithms outlined in the section titled 'Spatially-resolved MRT

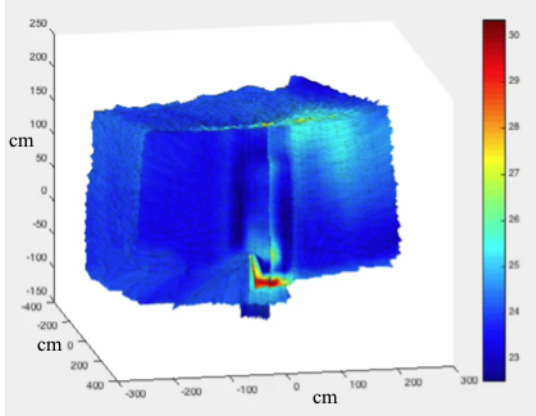


*Figure 6: Triangulation from the 3D point cloud (Fig. 5). A cold window with a radiator underneath is shown prominently in the foreground.*



*Figure 8: Photograph of the completed radiant cooling pavilion known as the Thermoheliadome.*

Calculation', which initially assumes no occluded regions in the floorplan. This type of MRT dataset is a requirement for precisely determining thermal comfort for building occupants, yet is inaccessible with current technology. The level of detail provided by the SMART sensor would allow for better control of radiant systems based on occupant locations and wall and window features in a space. Likewise, deficiencies in the radiant component of an occupant's thermal comfort could be compensated for with conventional systems, such as fans on one's desk or even intelligent chairs (Pasut et al., 2015). Sensing of occupants is possible with this sensor as well, and can offer additional energy savings from simply more intelligently controlling building systems with a MRT input.

## Discussion

The sensor was initially developed to measure the mean radiant temperature inside an outdoor radiant cooling pavilion known as the Thermoheliadome (Calabro et al., 2015; Read et al., 2015), shown in figure 8. The Thermoheliadome was plumbed with highly emissive pipes circulating evaporatively chilled water. The surface temperature of the pipes were reflected towards the center of the dome, thereby radiantly cooling an occupant positioned inside via reflected radiation. Since the structure was positioned outdoors in the summer, a black globe thermometer was subject to convective gains that were difficult to eliminate. Additionally, the obscure geometry of the structure made surface averaging difficult, so the SMART sensor was devised as a robust solution to MRT measurement. A point cloud of the Thermoheliadome's SMART sensor output is shown in figure 9.

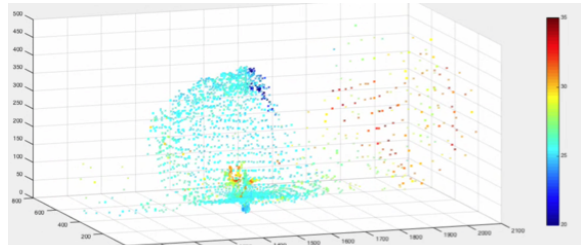


*Figure 9: A 3D point cloud of the Thermoheliadome.*

The sensor was used successfully to capture a spatially dependent MRT description of the space inside the Thermoheliadome, shown in figure 10. Here, the 20x20 grid used to calculate the MRT was generated by the range of the x and y coordinates, which for such a system is faulty. The results may only be interpreted inside of the dome. This issue highlights general occlusion issues with this type of optical sensing device, and may be accounted for by introducing a second sensor calibrated spatially to the first, or producing another image set after moving the first sensor. These are ongoing research projects, but would be important to more accurately build up a 3D point cloud in a room, accounting for occluded surfaces with a single sensor.

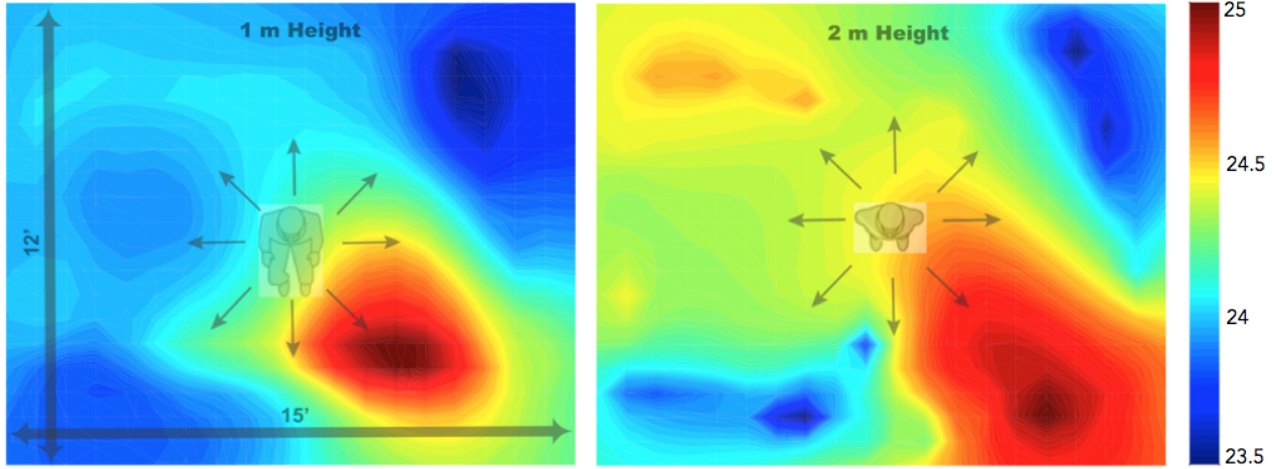


Figure 7: MRT calculated on a  $20 \times 20$  grid within the room at 1m and 2m heights. An occupant was added for a sense of when these two thermal environments would be perceived.

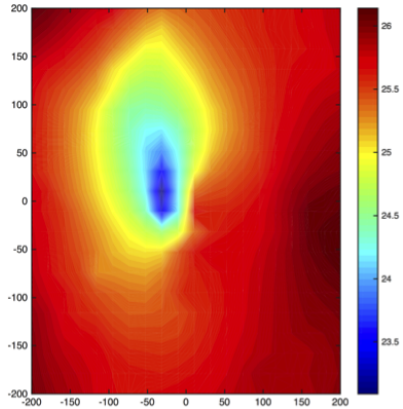


Figure 10: The MRT inside of the Thermoheliadome.

The environment the sensor is used in will also dictate how successful a single sensor would be versus many. For instance, a single sensor would be effective in a cubicle environment with radiantly activated walls. However, on the open-plan office scale, likely multiple sensors would be required.

We envision multiple versions of the sensor being deployed, one with a Lidar range-finding element, and the other without. The sensor without Lidar, pictured in figure 11, would be smaller, faster, and easier to integrate into an office environment to augment the limited air temperature data from thermostats. It would work in conjunction with the Lidar based version, whereby the 3D spatial information is scanned during a commissioning process, and that 3D data is stored with the temperature information being continually updated by the sensor without Lidar permanently mounted in the office to reduce cost and complexity. The CAD drawings could alternatively be used to provide 3D data for the room, but a diagnostic LIDAR scan would be able to provide additional info about installed furniture and other unexpected items like plants. To address size and noise of servo systems, this sensor could work with a galvanometer

system, moving small mirrors rather than a sensor element. We envision these future developments as improvements required for making the device deployable and eventually integrated into a building management system.

### Future Work

One potential issue that needs further consideration is gaps in the measured dataset. For instance, the circular FOV of the temperature sensor captures a significant portion of the overall imaginary  $8\pi$  steradians around the sensor, however there are small gaps. A sensitivity analysis based on the size of these gaps as a function of distance to a feature should be performed as part of a future study.

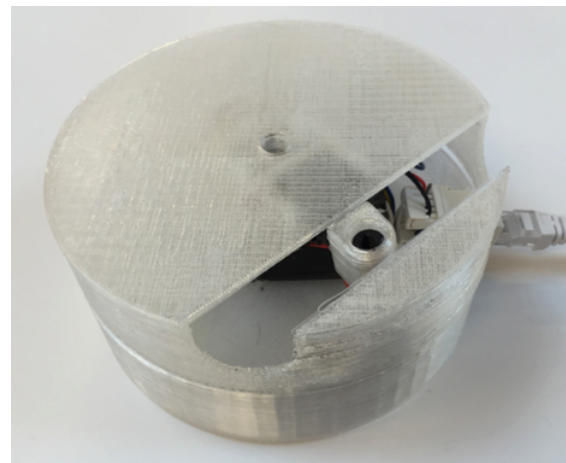


Figure 11: The SMART Sensor without Lidar.

As it stands, the computational algorithms that calculate the spatial MRT are slow. A first approach to reduce the computational time would be to identify surfaces, rather than use the point cloud. The triangular mesh currently used could in the future be modified to form contiguous non-overlapping faces joined together along their edges. To reduce

the computational cost or more explicitly the computational time, it is important that we create a mesh that contains vertices, edges and faces that are simpler, but maintains appropriate levels of details (Fabio, 2003).

There are currently commercial software packages that have the capability of accomplishing said tasks such as the Autodesk ReCap that takes the scanning results acquired by 3D laser scanners, creating 3D representations of existing structures. The point clouds however, remain computationally expensive, and contain an abundance of data, much of which is unnecessary for the amount of detail that is required for the understanding of the radiant environment. Additionally, work is being conducted using machine learning algorithms to teach computers to find planes in the context of viability for solar panel installations (Assouline et al., 2015). Similar techniques may be a strategy to first identify planes in the point cloud mesh, before the computationally intensive procedure of calculating view factors for thousands of very small triangles.

Another potential approach to simplify the point clouds could be segmenting the point clouds through analyzing the density of points - similarity of the point density potentially hints at planar surface, hence the point(s) that sees the change of point density might or could be understood as edges of surfaces of the measured space. More specifically, point density can be achieved through the calculation of the distance in Cartesian space through the angle and distance read through the range finder. So that if there is a sudden change of distances, it is possible that an ‘edge’ showed up. Averaging the surface temperature of the points with similar density could hence lead to much decreased computational costs that could have otherwise compromised the amount of work that is being done. This will definitely be a step up from the studies of Heath et al. (1998), Jiang and Bunke (1999) as well as Sappa and Devy’s work (2001), however shares similar concerns where converting Lidar data into range image (such as Digital Surface Model) could lead to significant information loss.

## Conclusion

The SMART sensor represents an exciting new approach to measuring the MRT within an environment, providing unprecedented levels of spatial detail and resolution. We have demonstrated results from a single sensor and post-processing algorithms that calculate the MRT at any point within the space. The outputs have implications for radiant systems controls, occupant thermal comfort, and outdoor MRT measurements, and can be refined computationally for use in many building and urban applications. Future work will investigate making the system more

deployable, with a focus on BMS integration.

## References

- Aagard, R. L. (1958). Convection Free Instrument for Measuring Infrared Radiation in the Atmosphere. *Review of Scientific Instruments* 29(11), 1011–1016.
- Assouline, D., N. Mohajeri, and J.-L. Scartezzini (2015). A machine learning methodology for estimating roof-top photovoltaic solar energy potential in switzerland. In *Proceedings of International Conference CISBAT 2015 Future Buildings and Districts Sustainability from Nano to Urban Scale*, Number EPFL-CONF-213375, pp. 555–560. LESO-PB, EPFL.
- Bedford, T and Warner, C G (2009, May). The Globe Thermometer in Studies of Heating and Ventilation. *Journal of Hygiene* 34(04), 458–473.
- Berglund, L. G. (1977, February). Radiation Measurement for Thermal Comfort Assessment in the Built Environment. *Symposium at the National Bureau of Standards*, 117–134.
- Calabrò, E., G. Aschwanden, N. Houchois, E. Teitelbaum, and F. Meggers (2015). Thermoheliometer testing: Evaluation methods for testing directed radiant heat reflection. In *Proceedings of 6th International Building Physics Conference, IBPC*.
- Fabio, R. (2003, December). From Point Cloud to Surface: The modeling and Visualization Problem. *International Archives of the Photogrammetry, Remote Sensing and Spatial Information Sciences*, 1–11.
- Fanger, P. O. (1970). Thermal comfort. analysis and applications in environmental engineering. *Thermal comfort. Analysis and applications in environmental engineering..*
- Gagge, A. P., J. Stolwick, and J. D. Hardy (1967). Comfort and Thermal Sensations and Associated Physiological Responses at Various Ambient Temperatures. *Environmental Research* 1(1), 1–20.
- Hager, N. E. (1963). Absolute Differential Radiometer. *Review of Scientific Instruments* 34(9), 1028–1034.
- Halawa, Edward, van Hoof, Joost, and Soebarto, Veronica (2014, September). The impacts of the thermal radiation field on thermal comfort, energy consumption and control—A critical overview. *Renewable and Sustainable Energy Reviews* 37, 907–918.
- Heath, M., S. Sarkar, T. Sanocki, and K. Bowyer (1998). Comparison of edge detectors: a methodology and initial study. In *IEEE Conference on Com-*

- puter Vision and Pattern Recognition, pp. 143–148. IEEE Comput. Soc. Press.
- Jiang, X. and H. Bunke (1999, February). Edge Detection in Range Images Based on Scan Line Approximation. *Computer Vision and Image Understanding* 73(2), 183–199.
- Koch, W. (1961, December). A Method of Calibrating Two-Sphere Non-directional Radiometers. *Nature* 192(4806), 960–960.
- Korsgaard, V (1949, September). Necessity of using a directional mean radiant temperature to describe the thermal conditions in rooms. *Heating, Piping and Air Conditioning* 21, 117–129.
- Lidwell, O. M. and D. P. Wyon (1968, May). A rapid response radiometer for the estimation of mean radiant temperature in environmental studies. *Journal of Physics E: Scientific Instruments* 1(5), 534–538.
- Lin, B., Z. Wang, H. Sun, Y. Zhu, and Q. Ouyang (2016). Evaluation and comparison of thermal comfort of convective and radiant heating terminals in office buildings. *Building and Environment*.
- McIntyre, D. A. (1976, May). A polyethylene shielded globe thermometer. *NASA STI/Recon Technical Report N* 78.
- Pasut, W., H. Zhang, E. Arens, and Y. Zhai (2015). Energy-efficient comfort with a heated/-cooled chair: Results from human subject tests. *Building and Environment* 84, 10–21.
- Read, J. R., F. Meggers, N. Houchois, G. Aschwanden, E. Teitelbaum, S. Adriaenssens, L. G. Rhode-Barbarigos, Y. Anastas, S. Coffers, and J. Pantelic (2015). Thermoheliodome design, optimization and fabrication. *Energy Procedia* 78, 273–278.
- Richards, C. H., A. M. Stoll, and J. D. Hardy (1951). The Panradiometer: An Absolute Measuring Instrument for Environmental Radiation. *Review of Scientific Instruments* 22(12), 925.
- Rupp, R. F., N. G. Vásquez, and R. Lamberts (2015). A review of human thermal comfort in the built environment. *Energy and Buildings* 105, 178–205.
- Sappa, A. D. and M. Devy (2001, January). Fast range image segmentation by an edge detection strategy. In *Third International Conference on 3-D Digital Imaging and Modeling*, pp. 292–299. Laboratoire d'Analyse et d'Architecture des Systèmes, Toulouse, France: IEEE Comput. Soc.
- Spagnolo, J. and R. De Dear (2003). A field study of thermal comfort in outdoor and semi-outdoor environments in subtropical sydney australia. *Building and environment* 38(5), 721–738.
- Thorsson, S., F. Lindberg, I. Eliasson, and B. Holmer (2007). Different methods for estimating the mean radiant temperature in an outdoor urban setting. *International Journal of Climatology* 27(14), 1983–1993.